Binary-phase Acetonitrile and Water Aerosols: Infrared Studies and Theoretical Simulation at Titan Atmosphere Conditions (SUPPORTING INFORMATION)

Rebecca Auchettl,[†] Mahmut Ruzi,[†] Dominique R. T. Appadoo,[‡] Evan G. Robertson,[†] and Courtney Ennis,*[†]

[†] Department of Chemistry and Physics, La Trobe Institute for Molecular Science, La Trobe University, Victoria, 3086, Australia. *c.ennis@latrobe.edu.au

[‡] Australian Synchrotron, 800 Blackburn Road, Clayton, Victoria, 3148, Australia.

S-1: Discrete Dipole Approximation

Discrete Dipole Approximation (DDA) is a model for the light scattering interaction with dielectric particles.[1] The 'target particle' can be of any shape (spherical and non-spherical) and architecture (e.g. pure or core-shell). A cubic array of equally spaced point dipoles, N, with inter-dipole spacing,d_i, simplifies the target particle. The bulk properties such as the refractive indices data are applied to each point dipole that makes up the target particle array.

Each individual dipole (i) has an instantaneous polarization (P_i) that makes up each sub-volume of the target particle where $\propto_i$ is the polarizability is tensor and $E_{loc}(r_i)$ is the instantaneous electric field at point r_i such that

$$P_i = \propto_i E_{loc}(r_i) \tag{2.1}$$

where P_i is determined at every N point on the cubic array and from the induced polarization. The value of P_i is then input into the standard optical theorems to calculate the extinction, absorption and scattering cross-sections.

The input data for these calculations come from the dielectric functions (ϵ) or the refractive index (n, k) of the substance which are related by the expressions:

$$(n,k)^2 = \epsilon \tag{2.2}$$

such that,

$$(n,k)^2 = n + i\kappa \tag{2.3}$$

$$\epsilon = \epsilon' + i\epsilon'' \tag{2.4}$$

where $\epsilon'$is the real dielectric function, $\epsilon''$is the imaginary component of the dielectric function, n is the real component of the refractive index, κ is the complex component of the refractive index and i is the complex number.

DDA requires several validity criteria to be satisfied in order to obtain accurate particle absorption spectra. These are:

(i) Number of dipoles, *N*, must be large enough to represent the target particle such that:

$$N > \frac{4\pi}{3}|n*|^3 \frac{2\pi}{\lambda}\alpha_{eff} \tag{2.5}$$

(ii) The interdipole spacing is smaller than the wavelength such that:

$$\frac{2\pi|m|d_s}{\lambda} < 1 \tag{2.6}$$

(iii) The interdipole spacing is smaller than the particle dimensions such that:

$$\propto_{eff} = \sqrt[3]{\frac{3V}{4\pi}} \tag{2.7}$$

$$VV = Nd_s^3 \tag{2.8}$$

As outlined by Preston and Signorell[2], the DDA approach can be applied to reproduce spectra for various molecular systems at higher efficiency than more computationally demanding methods. The disadvantage of using DDA is that the method relies on the availability of accurate refractive

indices (real and imaginary) spanning the frequency range of interest. Hence, the quality of the theoretical approximation depends on the quality of refractive indices; most often sourced from thin film experiments. If there is no refractive indices available, structural data can be used to derive model unit cells acting as coupled oscillators (known as the vibrational exciton model). Otherwise, from computational methods such as density functional theory using the experimentally extracted crystal structure obtained from powder diffraction experiments, the frequency dependent dielectric constants can be extracted from the crystal structure and which are then used as inputs for calculations. The vibrational exciton model methodology is preferable when the crystal is metastable or when the phase is unknown as there no dependent input data required other than transition dipole moments, molecular transition wavenumbers and the polarizability tensor.

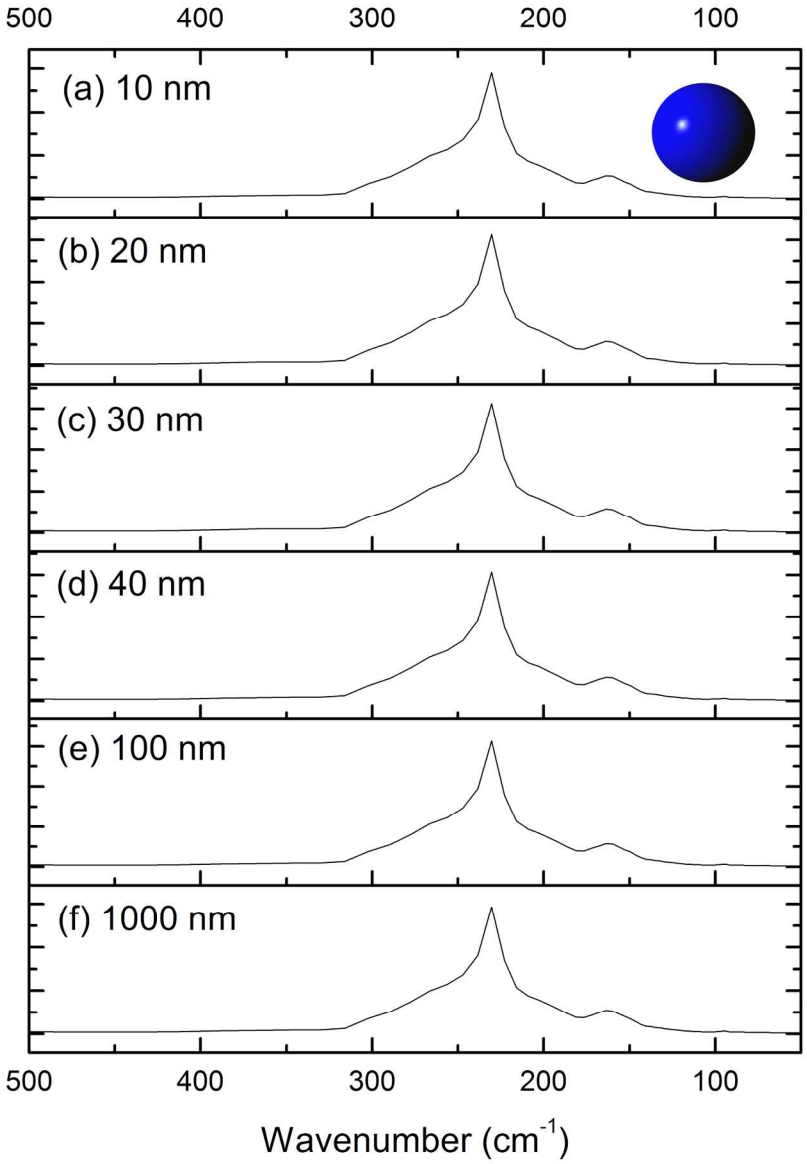

Figure S-1: Discrete dipole approximation far-IR spectra for H_2O I_c spherical aerosols with particle diameter (a) 10, (b) 20, (c) 30, (d) 40, (e) 100 and (f) 1000 nm.

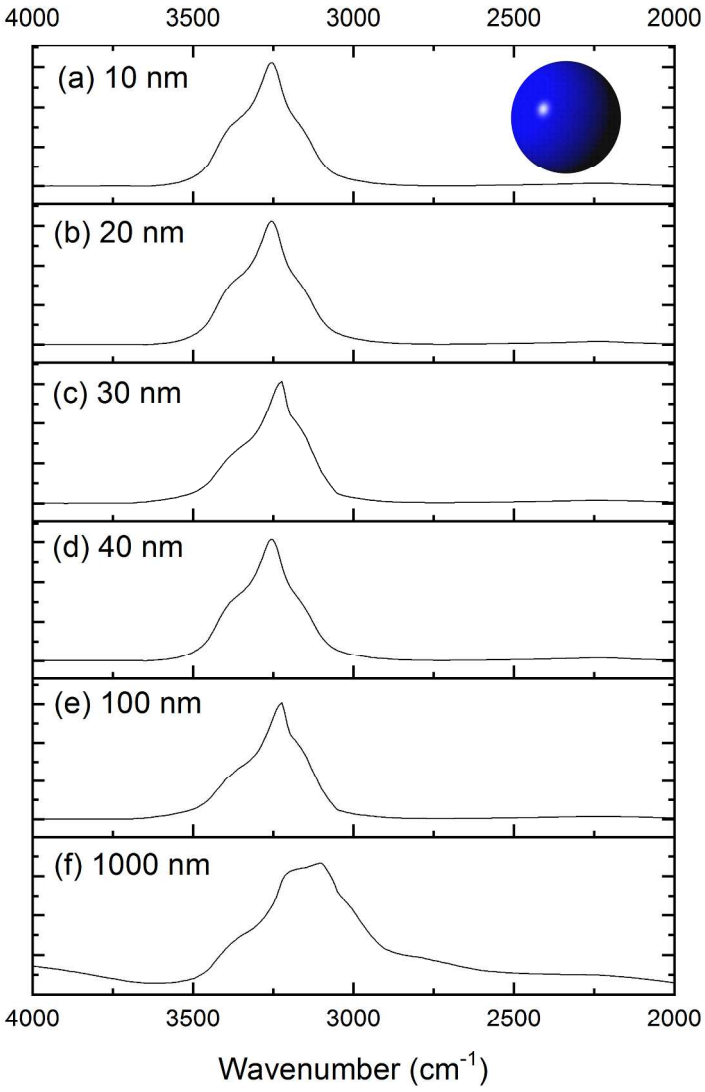

Figure S-2: Discrete dipole approximation mid-IR spectra for spherical particles of I_c phase H_2O with diameter (a) 10, (b) 20, (c) 30, (d) 40, (e) 100 and (f) 1000 nm.

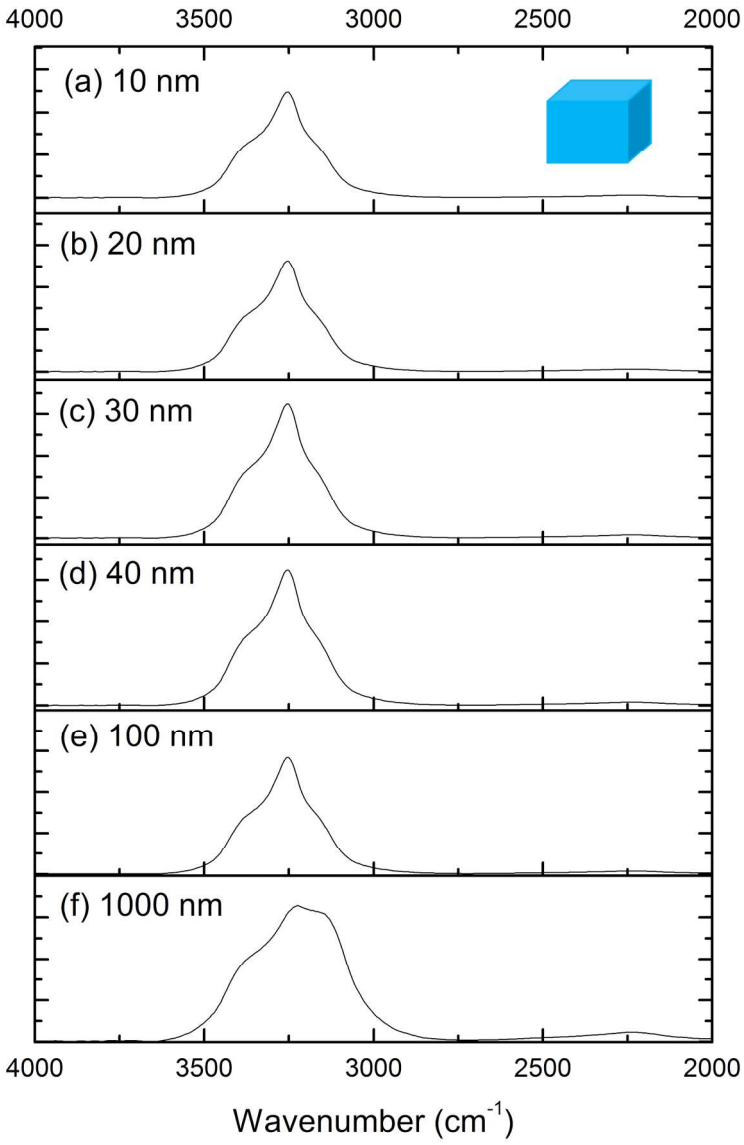

Figure S-3: Discrete dipole approximation mid-IR spectra for cube shaped particles of I_c phase H_2O with dimension (a) 10, (b) 20, (c) 30, (d) 40, (e) 100 and (f) 1000 nm.

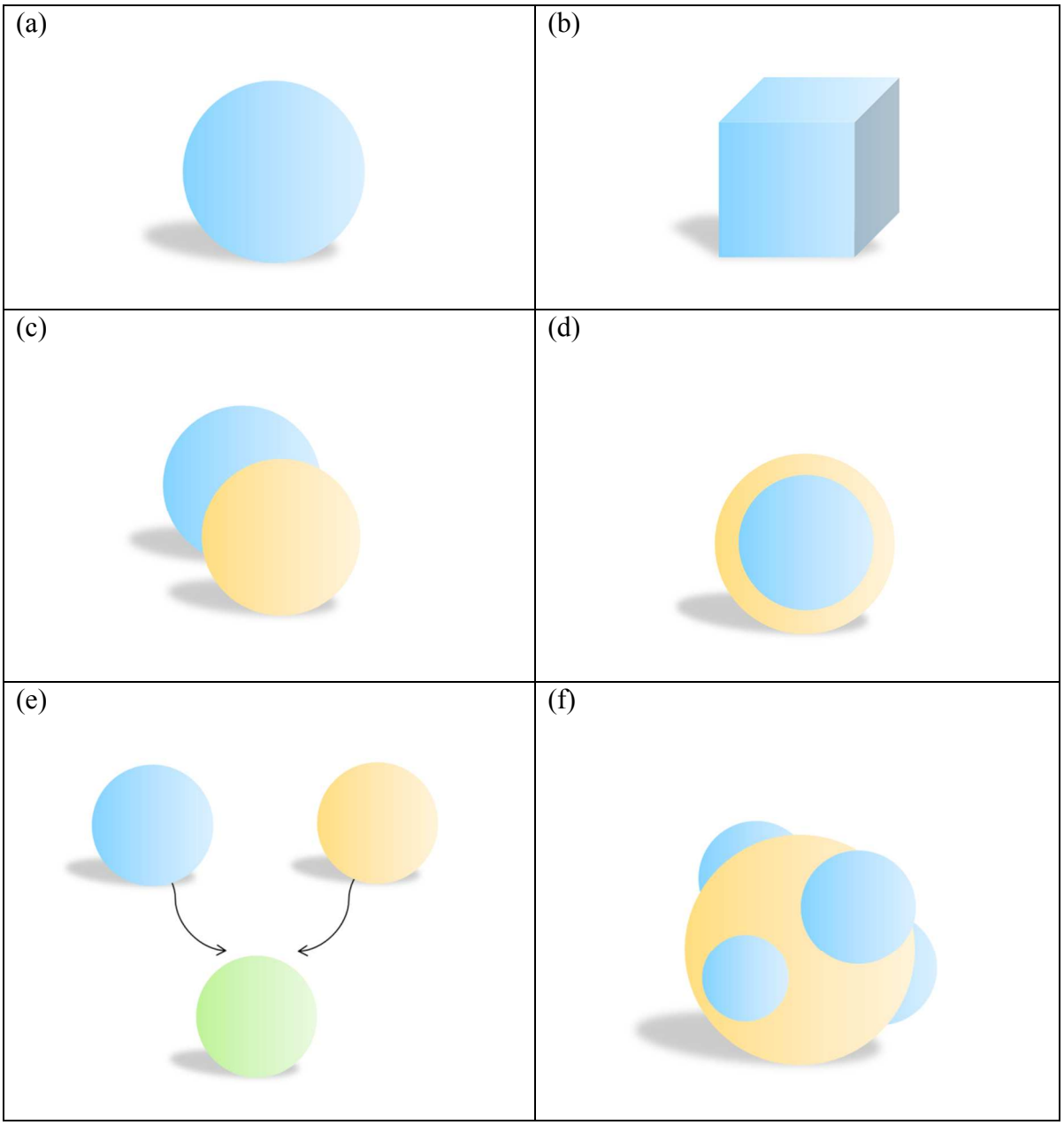

Figure S-4: Generalized aerosol shapes and architectures (a) spherical, (b) cube, (c) contact freezing with single interface, (d) core-shell, (e) molecularly mixed ("coalesced") and (f) engulfed contact freezing with multiple interfaces.

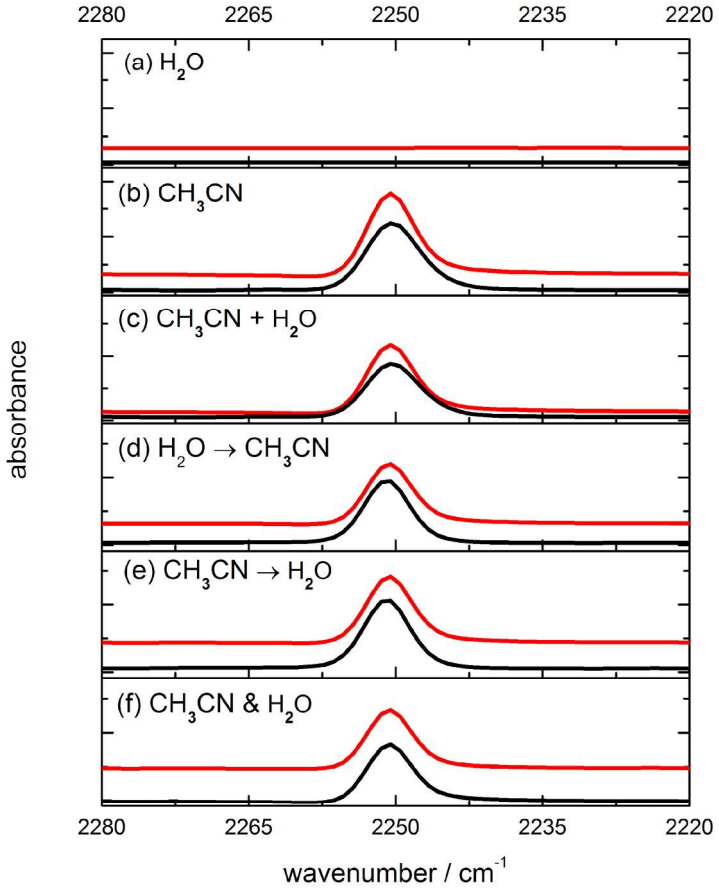

Figure S-5: Experimental mid-IR spectra (2280-2220 cm^{-1}) at 90 K (black) and 130 K (red) for the C≡N stretch region of (a) pure H_2O, (b) pure CH_3CN, (c) 1:3 CH_3CN-H_2O summation, (d) H_2O-injected first, (e) CH_3CN injected first, and (f) simultaneously deposited CH_3CN-H_2O aerosols with mol fraction x(CH_3CN) = 0.3.

(a) CH_3CN dimer – zig-zag configuration

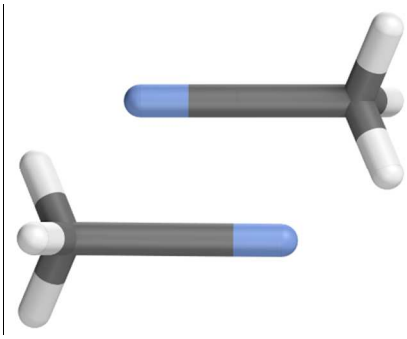

(b) Linear $CH_3CN\cdots H_2O$ complex

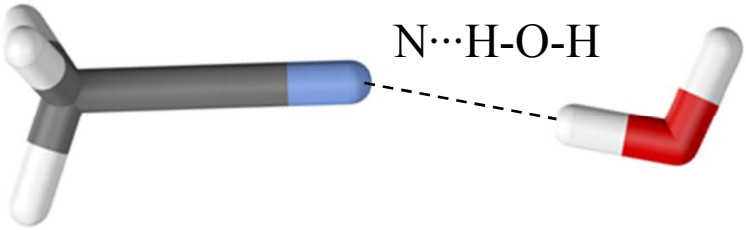

(c) Side-directed $CH_3CN\cdots H_2O$ complex

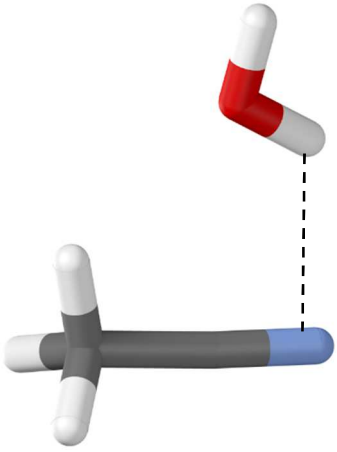

(d) $H_2O\cdots HOH$ dimer complex

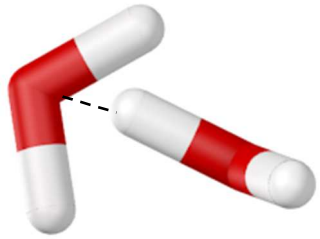

(e) Free CH_3CN complex with $(H_2O)_2$-$(CH_3CN)_2$

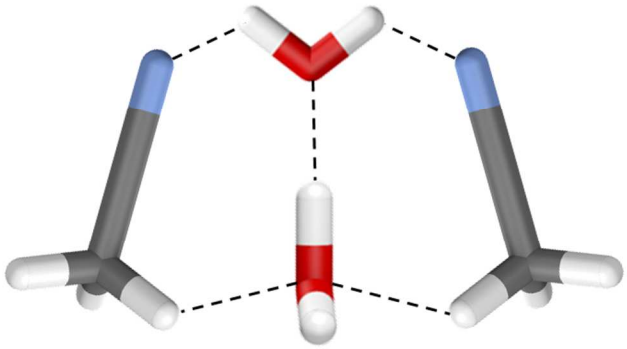

Figure S-6: Structures for (a) antiparallel zig-zag $CH_3CN\cdots CH_3CN$, (b) linear $CH_3CN\cdots HOH$ dimers, (c) side-directed $CH_3CN\cdots HOH$ complex, (d) $H_2O\cdots HOH$ dimer and (e) Free CH_3CN complex with $(H_2O)_2$-$(CH_3CN)_2$.

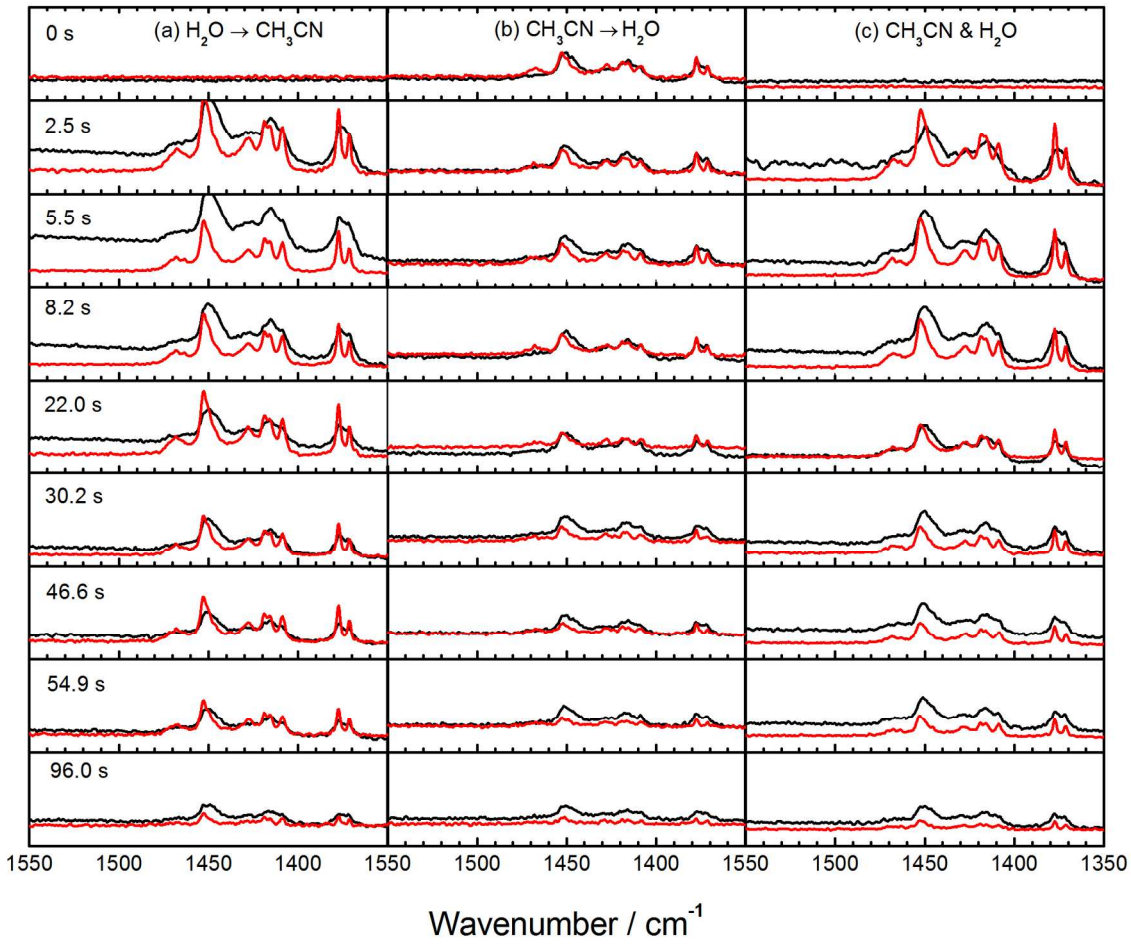

Figure S-7: Temporal mid-IR spectra (1550-1350 cm^{-1}) for (a) H_2O-injected first, (b) CH_3CN injected first (x4 intensity scaling), and (c) simultaneously deposited CH_3CN-H_2O aerosols at 100 K (black) and 130 K (red). Pulse width was 300 ms and delay between pulses was 500 ms.

Table S-1: Mid- and Far-IR vibrational bands for H_2O deposited as pure ice and in binary-phase H_2O-CH_3CN aerosols at 100 K (130 K). The modes labeled [2(SL)], [3(W)] and [4(SH)] are based on the phonon like assignment by Buch and Devlin, 1999[3] and Shi et al., 2012[4]. Peak positions are calculated using the second derivative method to identify the peak minimum.

		Literature Pure H_2O		H_2O	H_2O □ CH_3CN	CH_3CN □ H_2O	CH_3CN & H_2O
Mode[a, b, f]	Assignment[a, b]	Amorphous (IV) Thin Film[a] (cm^{-1})	Aerosol (cm^{-1})	Aerosol (cm^{-1})	Aerosol (cm^{-1})	Aerosol (cm^{-1})	Aerosol (cm^{-1})
dOH	Dangling O-H	-	3676[c]	3691 (3691)	3658 (3657)	3657 (3657)	3657 (3657)
		-	-	no	3618 (3617)	3619 (3618)	3618 (3618)
ν1, ν3 [4(SH)]	O-H sym. Stretch	3367	-	3368 (3379)	3370 (3370)	3362 (3376)	3371 (3368)
ν3 [3(W)]	Asym. stretch	3253	3257[e]	3231 (3232)	3227 (3234)	3227 (3231)	3226 (3230)
ν1 in-phase [2(SL)]	Sym. Stretch	3191	-	3129 (3137)	3127 (3135)	3131 (3135)	3130 (3135)
ν1 + ν3	Combination	2220	-	2232 (2233)	2251 (2251)	2251 (2250)	2251 (2250)
ν2	O-H bend	1660	1650[d]	1651 (1649)	1652 (1654)	1650 (1648)	1654 (1645)
νL	Libration	846	860[d]	856 (854)	854 (856)	854 (851)	854 (853)
νTO	Transverse Optic	213	232[d]	231 (230)	230 (229)	230 (229)	230 (229)
νLA	Longitudinal Acoustic	-	162[d]	170 (162)	161 (151)	162 (159)	161 (158)

no: not observed

(a) Hardin and Harvey, 1973[5]

(b) Whalley, 1977[6]

(c) Devlin et al., 2001[7]

(d) Medcraft et al., 2013[8]

(e) Isenor and Signorell, 2014[9]

(f) Shi et al., 2012[4]

Table S-2: Mid- and Far-IR vibrational bands for CH_3CN deposited as pure ice and in binary-phase H_2O-CH_3CN aerosols at 95 K (130 K). Peak positions are calculated using the second derivative method to identify the peak minimum.

Mode	Assignment	Literature Pure CH_3CN Thin Film (95 K)[g] (cm^{-1})	CH_3CN Aerosol (cm^{-1})	H_2O □ CH_3CN Aerosol (cm^{-1})	CH_3CN □ H_2O Aerosol (cm^{-1})	CH_3CN & H_2O Aerosol (cm^{-1})
$\nu_2 + \nu_4$	combination	3161[h]	3162 (3162)	3163 (3163)	3163 (3163)	3163 (3163)
ν_5	CH_3 asym. stretch	3000	3000 (3000)	3001 (3001)	3001 (3001)	3001 (3001)
ν_1	CH_3 sym. stretch	2939	2940 (2940)	2940 (2940)	2940 (2940)	2940 (2940)
			2737 (2737)	2737 (2737)	2737 (2737)	2737 (2737)
$\nu_2 + \nu_8$	combination	2628[i]	2633 (2635)	2634 (2634)	2634 (2634)	2634 (2634)
$\nu_6 + \nu_7$	combination	2486[i]	2486 (no)	2482 (2482)	2482 (2482)	2483 (2482)
			2447 (2446)	2447 (2447)	2447 (2447)	2447 (2447)
$\nu_3 + \nu_7$	combination	2414[h]	2412 (2413)	2413 (2413)	2413 (2413)	2413 (2413)
	CO_2		2343 (2340)	2357, 2344 (no)	2357, 2344 (no)	2358, 2344 (no)
$\nu_3 + \nu_4$	combination	2293[h]	2294 (2294)	2295 (2294)	2295 (2294)	2295 (2294)
ν_2	C≡N stretch	2251 (2247 sh)	2250 (2251)	2251 (2251)	2251 (2251)	2251 (2251)
$2\nu_4$	overtone	1834[i]	no (1830)	1829 (1829)	1829 (1829)	1829 (1829)
	HCOOH	no	1712 (1717)	no	no	no
$\nu_7 + \nu_8$	combination	1454	1453 (no)	no	no	no
		1451 (1448 sh)	1451 (1452)	1453 (1452)	1453 (1452)	1453 (1452)
ν_6	CH_3 deform.	1420	1420 (1418)	1418 (1418)	1418 (1418)	1418 (1418)
		1408	1409 (1409)	1409 (1409)	1409 (1409)	1409 (1409)
ν_3	CH_3 deform.	1378	1378 (1377)	1378 (1377)	1378 (1377)	1378 (1377)
		1372 (1368 sh)	1372 (1372)	1372 (1372)	1372 (1372)	1372 (1372)
		1049	1048 (1047)	1048 (1047)	1047 (1047)	1048 (1047)
ν_7	CH_3 rock	1040	no	no	no	no
		1036 (1032 sh)	1038 (1037)	1037 (1037)	1037 (1037)	1037 (1037)

ν_4	C-C stretch	915 (918 sh)	918 (918)	918 (918)	918 (918)	918 (918)
$2\nu_8$	overtone	774	773 (772)	773 (772)	770 (772)	773 (772)
ν_8	C-C≡N bend	393, 387	392, 385 (392, 385)	387 (392, 385)	386 (393, 385)	386 (391, 385)
$\nu\mathbf{L_T}$	Translational	123	132 (125)	131 (128)	129 (129)	130 (126)
$\nu\mathbf{L_{XY}}$	Librational	91	93 (90)	95 (89)	94 (89)	86 (88)

no: not observed
(g) Dello Russo and Khanna, 1996[10]
(h) Pace and Noe, 1968[11]
(i) Parker et al., 1957[12]

Table S-3: H_2O OH stretch peak (cm^{-1}) and dangling OH (dOH) peak position (cm^{-1}) with corresponding integrated areas with calculated particle diameters for pure H_2O experiments at 100 K to 130 K and 100 mbar buffer pressure. H_2O particle size is calculated from the ratio of the integrated intensity of the OH stretch to the dOH.[13]

Temp (K)	OH (cm^{-1})	Area $_{OH}$	dOH (cm^{-1})	Area $_{dOH}$	Size (nm)
130 K	3236	54.4	3691	0.013	28
100 K	3231	44.3	3691	0.015	20

Table S-4: Peak frequency shifts (δν) from the pure-phase absorption band for three deposition techniques at 100 K (130 K). Peak positions are calculated using the second derivative method to identify the peak minimum.

Molecule	Mode	Assignment	Pure δν (cm^{-1})	H_2O □ CH_3CN δν (cm^{-1})	CH_3CN □ H_2O δν (cm^{-1})	CH_3CN & H_2O δν (cm^{-1})
H_2O	dOH	Dangling O-H	3691 (3691)	-34 (-33)	-34 (-34)	-34 (-34)
H_2O	ν1, ν3 [4(SH)]	O-H sym. Stretch	3368 (3379)	-2 (9)	6 (3)	-3 (11)
H_2O	ν3 [3(W)]	Asym. stretch	3231 (3232)	4 (-2)	4 (1)	5 (2)
H_2O	ν1 in-phase [2(SL)]	Sym. Stretch	3129 (3137)	2 (2)	-2 (2)	-1 (2)
H_2O	ν2	O-H bend (surface)	1651 (1649)	-1 (-5)	1 (1)	-3 (4)
H_2O	νLibration	Libration	856 (854)	2 (-2)	2 (3)	2 (1)
H_2O	νTO	Transverse Optic	231 (230)	1 (1)	1 (1)	1 (1)
H_2O	νLA	Longitudinal Acoustic	170 (162)	9 (11)	8 (3)	9 (4)
CH_3CN	$\nu_2 + \nu_4$	combination	3162 (3162)	-1 (-1)	-1 (-1)	-1 (-1)
CH_3CN	ν_5	CH_3 asym. stretch	3000 (3000)	-1 (-1)	-1 (-1)	-1 (-1)
CH_3CN	ν_1	CH_3 sym. stretch	2940 (2940)	0 (0)	0 (0)	0 (0)
CH_3CN	$\nu_3 + \nu_7$	combination	2412 (2413)	-1 (0)	-1 (0)	-1 (0)
CH_3CN	$\nu_3 + \nu_4$	combination	2294 (2294)	-1 (0)	-1 (0)	-1 (0)
CH_3CN	ν_2	C≡N stretch	2250 (2251)	-1 (0)	-1 (0)	-1 (0)
CH_3CN	ν_6	CH_3 deform.	1420 (1418)	2 (0)	2 (0)	2 (0)
CH_3CN	ν_4	C-C stretch	918 (918)	0 (0)	0 (0)	0 (0)
CH_3CN	$2\nu_8$	overtone	773 (772)	0 (0)	3 (0)	0 (0)
CH_3CN	ν_8	C-C≡N bend	392, 385 (392, 385)	-2 (0, 0)	-1 (-1, 0)	-1 (+1, 0)
CH_3CN	$\nu\mathbf{L_T}$	Translational	132 (125)	1 (-3)	3 (-4)	2 (-1)
CH_3CN	$\nu\mathbf{L_{XY}}$	Librational	93 (90)	-2 (1)	-1 (1)	7 (2)

Table S-5: Peak frequency shifts (δν) from 100 to 130 K for three deposition techniques at 100 mbar. Peak positions are calculated using the second derivative method to identify the peak minimum.

Molecule	Mode	Assignment	Pure δ (cm^{-1})	H_2O □ CH_3CN δ (cm^{-1})	CH_3CN □ H_2O δ (cm^{-1})	CH_3CN & H_2O δ (cm^{-1})
H_2O	dOH	Dangling O-H	0	1	0	0
H_2O	ν1, ν3 [4(SH)]	O-H sym. Stretch	11	0	14	-3
H_2O	ν3 [3(W)]	Asym. stretch	1	7	4	4
H_2O	ν1 in-phase [2(SL)]	Sym. Stretch	8	8	4	5
H_2O	ν2	O-H bend (surface)	-2	2	-2	-9
H_2O	νLibration	Libration	-2	2	-3	-1
H_2O	νTO	Transverse Optic	-1	-1	-1	-1
H_2O	νLA	Longitudinal Acoustic	-8	-10	-3	-3
CH_3CN	$\nu_2 + \nu_4$	combination	0	0	0	0
CH_3CN	ν_5	CH_3 asym. stretch	0	0	0	0
CH_3CN	ν_1	CH_3 sym. stretch	0	0	0	0
CH_3CN	$\nu_3 + \nu_7$	combination	1	0	0	0
CH_3CN	$\nu_3 + \nu_4$	combination	0	-1	-1	-1
CH_3CN	ν_2	C≡N stretch	1	0	0	0
CH_3CN	ν_6	CH_3 deform.	-2	0	0	0
CH_3CN	ν_4	C-C stretch	0	0	0	0
CH_3CN	$2\nu_8$	overtone	-1	-1	2	-1
CH_3CN	ν_8	C-C≡N bend	0, 0	no, -2	no, -1	no, -1
CH_3CN	$\nu\mathbf{L_T}$	Translational	-7	-3	0	-4
CH_3CN	$\nu\mathbf{L_{XY}}$	Librational	-3	-6	-5	2

Table S-6: Temporal far-IR band positions for (a) νLA(H_2O), (b) νTO(H_2O), (c) νL_T(CH_3CN), (d) νL_{XY}(CH_3CN) and (e) ν_8(CH_3CN) bands of binary-phase CH_3CN-H_2O aerosols at 130 K. Peak positions are calculated using the second derivative method to identify the peak minimum.

t / s	H_2O □ CH_3CN / cm^{-1}	CH_3CN □ H_2O / cm^{-1}	CH_3CN & H_2O / cm^{-1}
νLA(H_2O)			
0	169	-	-
1.7	167	-	168
5.0	168	169	no
8.3	166	160	no
10.0	? 171	157	171
11.6	160	178	no
νTO(H_2O)			
0	229	-	-
1.7	229	no	228
5.0	229	228	229
8.3	229	229	230
10.0	230	230	229
11.6	231	230	229
νL_T(CH_3CN)			
0	-	-	-
1.7	no	92	no
5.0	92	93	90
8.3	93	93	91
10.0	93	88	93
11.6	no	89	91
νL_{XY}(CH_3CN)			
0	-	-	-
1.7	130	129	126
5.0	130	126	127
8.3	127	127	127
10.0	128	126	128
11.6	129	127	126
ν_8 (CH_3CN)			
0	-	-	-
1.7	386	382	385
5.0	386/393	386	389
8.3	387	387	384
10.0	386/394	386	386
11.6	379/386	387	384/391

no: not observed

(1) Signorell, R. Verification of the Vibrational Exciton Approach for CO_2 and N_2O Nanoparticles. *J. Chem. Phys.* **2003**, *118* (6), 2707–2715.

(2) Preston, T. C.; Signorell, R. From Plasmon Spectra of Metallic to Vibron Spectra of Dielectric Nanoparticles. *Acc. Chem. Res.* **2012**, *45* (9), 1501–1510.

(3) Buch, V.; Devlin, J. P. A New Interpretation of the OH-Stretch Spectrum of Ice. *J. Chem. Phys.* **1999**, *110* (7), 3437–3443.

(4) Shi, L.; Gruenbaum, S. M.; Skinner, J. L. Interpretation of IR and Raman Line Shapes for H_2O and D_2O Ice Ih. *J. Phys. Chem. B* **2012**, *116* (47), 13821–13830.

(5) Hardin, A. H.; Harvey, K. B. Temperature Dependences of the Ice I Hydrogen Bond Spectral Shifts - I. The Vitreous to Cubic Ice I Phase Transformation. *Spectrochim. Acta Part A Mol. Spectrosc.* **1973**, *29* (6), 1139–1151.

(6) Whalley, E. A Detailed Assignment of the O–H Stretching Bands of Ice I. *Can. J. Chem.* **1977**, *55* (19), 3429–3441.

(7) Devlin, J. P. Structure, Spectra, and Mobility of Low-Pressure Ices: Ice I, Amorphous Solid Water, and Clathrate Hydrates at T < 150 K. *J. Geophys. Res. Planets* **2001**, *106* (E12), 33333–33349.

(8) Medcraft, C.; McNaughton, D.; Thompson, C. D.; Appadoo, D. R. T.; Bauerecker, S.; Robertson, E. G. Water Ice Nanoparticles: Size and Temperature Effects on the Mid-Infrared Spectrum. *Phys. Chem. Chem. Phys.* **2013**, 3630–3639.

(9) Isenor, M.; Signorell, R. Infrared Spectroscopy of Solid Mixed Ammonia–water and Acetylene–water Aerosol Particles. *Mol. Phys.* **2014**, *113* (8), 823–834.

(10) Dello Russo, N.; Khanna, R. K. Laboratory Infrared Spectroscopic Studies of Crystalline Nitriles with Relevance to Outer Planetary Systems. *Icarus* **1996**, *123* (2), 366–395.

(11) Pace, E. L.; Noe, L. J. Infrared Spectra of Acetonitrile and Acetonitrile-d_3. *J. Chem. Phys.* **1968**, *49* (12), 5317–5325.

(12) Parker, F. W.; Nielsen, A. H.; Fletcher, W. H. The Infrared Absorption Spectrum of Methyl Cyanide Vapor. *J. Mol. Spectrosc.* **1957**, *1* (1–4), 107–123.

(13) Devlin, J. P.; Sadlej, J.; Buch, V. Infrared Spectra of Large H_2O Clusters: New Understanding of the Elusive Bending Mode of Ice. *J. Phys. Chem. A* **2001**, *105* (6), 974–983.